WATER RESOURCES RESEARCH, VOL. 31, NO. 10, PAGES 2503–2515, OCTOBER 1995

The Great Salt Lake: A barometer of low-frequency climatic variability

Upmanu Lall
Utah Water Research Laboratory, Utah State University, Logan

Michael Mann
Department of Geology and Geophysics, Yale University, New Haven, Connecticut

Abstract. Low-frequency (interannual or longer period) climatic variability is of interest because of its significance for the understanding and prediction of protracted climatic anomalies. Closed basin lakes are sensitive to long-term climatic fluctuations and integrate out high-frequency variability. It is thus natural to examine the records of such lakes to better understand long-term climate dynamics. Here we use singular spectral analysis and multitaper spectral analysis to analyze the time series of Great Salt Lake (GSL) monthly volume change from 1848 to 1992 and monthly precipitation, temperature, and streamflow for nearby stations with 74 or more years of data. This analysis reveals high fractional variance in 15–18, 10–12, 3–7 and 2-year frequency bands, which seems to be consistent across time series. The putative decadal and interdecadal signals appear to be related to large-scale climate signals. The interannual signals are consistent with El Niño Southern Oscillation and quasi-biennial variability. Prospects for improved prediction of the GSL volume and of protracted wet/dry periods in the western United States are discussed.

Introduction

Our fascination with climatic cycles goes back as far as recorded history. Almost every possible periodicity between 2 and 200 years has been observed with some certainty [*Burroughs*, 1992, p. 60]. Burroughs also observes that "the history of meteorology is littered with the whitened bones of claims to have demonstrated the existence of reliable cycles in the weather." Often, the "cycle" is wont to disappear soon after its discovery and may spontaneously reappear later. The existence and understanding of all but the diurnal and the annual cycle are polemical.

The search for hidden order is one of science's aspirations. Moreover, given the social, economic, and geopolitical implications of successful long-term climatic forecasts, interest in the identification and explanation of recurrent climatic patterns is natural. Recently [see *Diaz and Pulwarty*, 1994; *Mann and Park*, 1993, 1994 (hereafter, MP93, MP94); *Houghton and Tourre*, 1992; *Currie and O'Brien*, 1992; *Ghil and Vautard*, 1991 (hereafter, GV); *Dettinger and Ghil*, 1991; *Trenberth*, 1990; *Levitus*, 1989], interest has focused on the possibility of decadal/interdecadal climatic variability that may be due to internal (e.g., ocean-atmosphere interaction) or external (e.g., sunspot cycles or lunar tides) factors. Indeed, GV and MP94 argue that a large part of the recent global warming may be explained as the superposition of distinct quasi-periodic climatic patterns with different frequencies. Can one explain droughts and other protracted anomalies similarly?

Recognition of low-frequency variability leads to changes in the interpretation (e.g., of water quality trends) and utility of hydroclimatic records. Traditional hydrologic models formulated at monthly or annual timescales assume stationarity of the statistics of the underlying process. Interannual structure in these time series invalidates such assumptions. The identification of coherent, low-frequency patterns is also relevant to interpretation of long-range persistence or the Hurst effect.

A purpose of the work presented here is to develop an empirical understanding of the role of climatic variability in the dynamics of the Great Salt Lake (GSL) of Utah, a closed lake in the arid western United States. Our findings are also directly relevant to the ongoing debate on interdecadal climatic variability. A long record (1848–1992) was available. The GSL "samples" precipitation in the Great Basin, an area where most of the precipitation occurs at high elevations and runoff is largely from snowmelt. Worldwide, very few long-record, high-elevation, precipitation gauges are available. *Barnston and van den Dool* [1993] suggest that regions with low interannual variance in atmospheric circulation are favorable sites for studying low-frequency climatic behavior. In their analysis of 700-mbar atmospheric pressure surface data, the GSL basin is such a region. Insights from spectral analyses using "modern" methods such as singular spectral analysis (SSA) [*Vautard et al.*, 1992], and the multitaper spectral analysis method (MTM) [*Thomson*, 1982] of GSL volume changes and precipitation, temperature, and streamflow time series at nearby stations are presented here (see Figure 1 for a site map and Table 1 for site information). Of interest is evidence for structured low-frequency variability in these time series and insight into the relative sensitivity of the GSL to low-frequency precipitation and temperature variability.

In the next section we develop a perspective for the analysis of climatic variability: Are cycles sustained; do they represent quasi-periodic transitions between different climatic regimes; or are they episodic damped oscillations triggered by external events? What are the implications for the analysis of a finite, noisy time series? What are some desirable attributes of the analysis methodology? Background information on the Great

Paper number 95WR01950.
0043-1397/95/95WR-01950$05.00

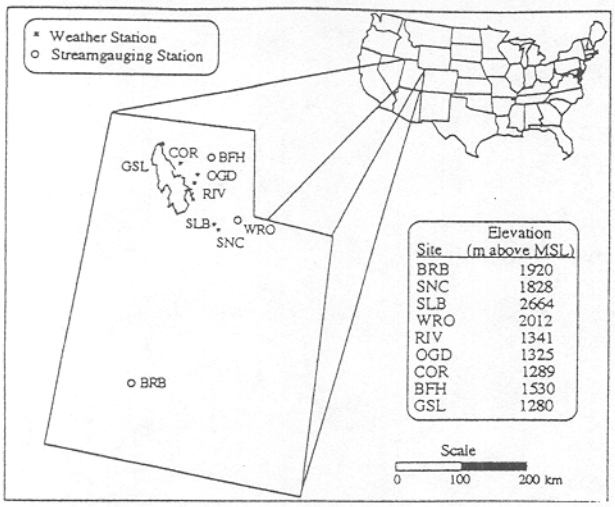

Figure 1. Site map.

Salt Lake and its environs comes next. A section describing the methods used follows. This leads to the results from the analysis of the selected time series.

Notions About Climatic Fluctuations and Data Analysis Issues

During 1983–1986 the Great Salt Lake rose rapidly to its highest level in a hundred years and then declined quickly just as a $60 million pumping project to control its level was implemented. The previous decade had seen concern that the GSL might be drying up. The persistent rain and floods in the Mississippi River basin in 1993 were equally noteworthy. Such extremes are fascinating because they occur at every timescale, and in human memory, with some regularity. Let us examine some postulates regarding such behavior.

The first postulate is that the climatic time series is the outcome of a random process (perhaps one with some memory) and the diurnal and annual cycles. The observed extremes occur randomly in accordance with such a process. This is a rather unsatisfying postulate, not in the least because it provides little physical intuition or understanding of the climatic process.

Pragmatically, it is known that a number of deterministic and chaotic systems [*Abarbanel et al.*, 1993] have generally broadband spectra that can be easily misclassified as "white" or "red" noise systems. The underlying dynamics may have well-defined regimes with nearly periodic transitions between them at some preferred range of timescales. Predictability is lost only by passage through some unstable state(s). Consequently, there are no sharp spectral peaks, but possibly high power in some frequency bands that will be overlooked in a traditional periodogram analysis. Since it calls for an explanation, evidence of such frequency structure in the spectrum of climatic time series is important, even if no sharp spectral peaks are apparent. There is a growing recognition [e.g., *Kahya and Dracup*, 1993; *Guetter and Georgakakos*, 1993; *Cayan and Webb*, 1992; *Cayan and Peterson*, 1989; *Ropelewski and Halpert*, 1987] of the importance of the nearly periodic (over 2- to 3-year and 4- to 6-year frequency bands) El Niño Southern Oscillation (ENSO) on temperature, precipitation, and streamflow variability over large regions.

The second postulate is that the climate system is deterministic, with positive and negative feedbacks that lead to recurrent patterns in time and space. Such "oscillations" may be described by linear or nonlinear dynamics associated with the amplifying (positive) and restoring (negative) forces. The governing equations (see *Lorenz* [1976] or *Saltzman* [1983]) of the climate system are nonlinear with a variety of feedbacks. What are some implications of nonlinearity that are of interest in analyzing climatic time series?

Harmonic generation. *Burroughs* [1992, p. 147], indicates that in a nonlinear system, (1) higher harmonics (e.g., $2f$, $3f$, etc.) of an external forcing at frequency f may be generated and (2) if there are two or more forcing frequencies, periodicities at integer combinations of these frequencies may show up in the response. In the latter case (often called a quasi-periodic system), low-frequency responses (e.g., through the

Table 1. Data Sets Analyzed

	Latitude	Longitude	Elevation, m above MSL	Record Length	Source	Comments
Great Salt Lake (GSL)	40°20′ to 41°40′N	111°52′ to 113°06′W	1280	1848–1991	USGS, *Sangoyomi* [1993]	monthly volume change
Snake Creek (SNC)	40°33′N	111°30′W	1828	1916–1989	*Fan and Duffy* [1993]	monthly temperature and precipitation
Silver Lake/Brighton (SLB)	40°36′N	111°35′W	2664*	1916–1989	*Fan and Duffy* [1993]	monthly precipitation
Riverdale (RIV)	41°09′N	112°00′W	1341	1916–1989	*Fan and Duffy* [1993]	monthly temperature and precipitation
Ogden (OGD)	41°15′N	111°57′W	1325	1916–1989	*Fan and Duffy* [1993]	monthly precipitation
Corinne (COR)†	41°33′N	112°07′W	1289‡	1902–1989	*Fan and Duffy* [1993]	monthly temperature and precipitation
Beaver River near Beaver (BRB)§	38°17′N	112°34′W§	1920	1915–1988	USGS, *Slack et al.* [1992]	monthly streamflow
Weber River near Oakley (WRO)	40°44′N	111°15′W	2012	1905–1988	USGS, *Slack et al.* [1992]	monthly streamflow
Blacksmith Fork near Hyrum (BFH)	41°37′N	111°44′W	1530	1919–1988	USGS, *Slack et al.* [1992]	monthly streamflow

MSL denotes mean sea level; USGS is U.S. Geological Survey.
*Highest station.
†Closest to GSL.
‡Lowest station.
§South of GSL drainage and does not flow into GSL.

combination f_1-f_2) may be generated. Typically, the amplitude of the higher harmonics is smaller than that of the lower harmonics. Once again, such a response could easily be misclassified as "red" noise upon periodogram analysis. *Sangoyomi* [1993] analyzed the spectrum of the biweekly 1848–1992 GSL volume using classical periodogram analysis following a recipe for peak identification suggested by *MacDonald* [1989], and found that there were 15 peaks that were significant at the 0.1 level. However, all these peaks could be resolved as integer combinations of four base frequencies corresponding to periods of 36.07, 14.23, 11.10, and 1 years. This is an interesting preamble for this work since it naturally raises the question of whether this quasi-periodicity is generated by the dynamics of the lake and its drainage or by climatic variability. *Jin et al.* [1994] develop a paradigm for ENSO along these lines.

Entrainment. *Burroughs* [1992, p. 148] describes entrainment as a situation in which a system with a natural self-excitation frequency f_1, if stimulated by a forcing at frequency f_2, may respond at f_2 if f_2 is close to f_1, or asynchronously, at a new frequency f_3. Transient oscillations in one part of the system (e.g., the ocean) may consequently lead to a synchronous or asynchronous response in other parts of the system. Energetic perturbations, such as volcanoes, may lead to oscillatory chain reactions. The affected subsystem may respond with a damped oscillation at its natural frequency. In a dissipative system, such a chain of events would eventually damp out. Weakly unstable periodic orbits (corresponding to internal or natural response frequencies) may attract trajectories intermittently and lead to spells of periodic activity. Such cycles may show up in one segment of the data but may be missing in another. Such variability will typically show up in a spectrum as an elevated narrow band rather than a sharp peak. ENSO is often assigned this interpretation. Thus the response of the system to particular forcings (e.g., volcanic disturbances) that occur at roughly the same state of the system may have short-term predictability. This observation may account for the success of U. Lall et al. (Nonlinear dynamics of the Great Salt Lake: Nonparametric short-term forecasting, submitted to *Water Resources Research*, 1995) in predicting the GSL for up to 4 years in the future using a nonlinear dynamics–based forecasting model.

Phase shift. Phase shifts relate to the previous discussion on entrainment. *Burroughs* [1992, p. 149] points out that for systems that are forced by a combination of frequencies that slowly move in and out of phase, the response of the climate at the higher frequency may suddenly switch its phase by π radians. This leads to a loss of predictability and identifiability unless such a phase shift can be anticipated or described. It also implies that the associated signal will most likely fail significance tests for phase coherence upon data analysis unless appropriately chosen data segments are looked at.

Research into interannual and interdecadal climatic mechanisms has received renewed impetus recently as it has become clear that (1) such features exist, (2) the amplitude of low-frequency oscillations is high, and (3) they are important to understand in the context of not only the global warming debate, but also the nature of climate in general. Of course, considerable controversy surrounds the data, the analysis, and the proposed mechanisms at this point. Typical cycles identified most often are 2.1, 3.1, 3.4, 3.7, 5.2, 6.9, 10, 11, 15, 18, 22, and 25 years [*Burroughs*, 1992]. In light of the discussion thus far, it is useful to think of such variability as organized by characteristic frequency bands rather than sharp peaks.

Clearly, nonlinearity imparts complexity, and by itself, the analysis of a finite data set is unlikely to resolve most of the features we list above. We hope to isolate at least some frequency bands where there is evidence of activity, as well as intermittent oscillations. It will also be instructive to see if the differences in the analyses of precipitation, temperature, streamflow, and GSL time series are consistent with one's expectations regarding the evolution of these processes. Specifically, do we see a relative filtering of the higher-frequency phenomena as we move through this sequence of series. Are there any new features introduced that may highlight the role of hydrologic processes?

Long records are essential for investigations into intermittent oscillations, phase shifts, and important frequency bands. What kind of record is most useful? Clearly, one must guard against making far-reaching conclusions from data at a single location, lest the feature be an artifact of the local circulation or systematic biases (e.g., due to man's activity or instrumental errors). On the other hand, MP93 show that the use of regionally or globally averaged data can lead to a cancelation of a spatially evolving pattern. Since the spatial distribution of recording stations is highly nonuniform over the Earth, working with the spatial data set may also implicitly introduce poorly quantifiable biases into the analysis. Carefully selected hydrologic records (streams, closed basin lakes) offer an opportunity to use "natural" averaging of the climatic signal. However, they may introduce artifacts (at the high-frequency range) that are peculiar to drainage basin hydrology, and they also suffer from nonstationarity induced by man's activity. Here, we use a number of local hydroclimatic records as a check for the self-consistency of the local/regional signal identified. Connections between the signals identified here and large-scale atmospheric circulation are explored further by *Mann et al.* [1995].

The Great Salt Lake and Data Used

Closed lakes occur in arid regions of the world, where there is a delicate hydrologic balance between the long-term average lake evaporation, precipitation, and runoff from the drainage basin. The average lake evaporation rate (volume/(time × area)) usually exceeds the average precipitation rate, and the difference is balanced by basin runoff. The drainage basin of the lake is topographically closed. The only outlet for water is evaporation, which is determined by temperature, relative humidity, lake area, wind, and salinity. Precipitation on the lake and runoff (induced by precipitation in the drainage basin) constitute lake inputs. Such lakes are of interest because (1) they are very sensitive to climatic variability, (2) their volumetric fluctuation represents a natural space and time average of regional climatic variability, and (3) they can highlight longer-term fluctuations through a natural damping of high-frequency components.

The GSL is the fourth largest (average surface area, 4350 km^2), first or second saltiest (salt 15–28% by weight), and shallowest (average depth 5 m) perennial closed lake in the world. The large surface area and shallow depth make the lake very sensitive to fluctuations in long-term evaporation and precipitation. The topographic relief in the basin ranges from the GSL elevation of 1280 m above mean sea level (MSL) to 3960 m above MSL. The principal mountain ranges as well as the primary influent rivers are east of the lake. The drainage

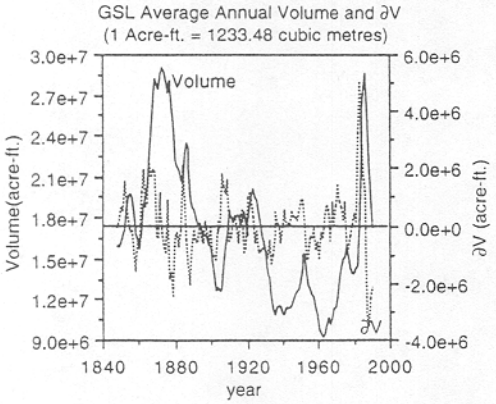

Figure 2. GSL annual volume and annual volume change time series (1848–1991).

area of the lake is approximately 90,000 km^2, of which approximately 40% does not contribute flow to the lake except under very wet conditions (e.g., 1983–1986). Low levels of the GSL correspond to regional drought. High levels of the GSL in the 1980s led to extensive flooding and damage. A volumetric record (Figure 2) from 1848–1992 developed by *Sangoyomi* [1993] is used here. The variables analyzed are the monthly and annual GSL average volume change. We choose the differenced volume, rather than the volume itself, to allow an easier comparison with the precipitation, temperature, and streamflow records. While such differencing could introduce noise at frequencies near the monthly sampling, it does not significantly alter the attributes of low-frequency periodic structure.

Monthly temperature and precipitation records [see *Fan and Duffy*, 1993] for five sites (Silver Lake–Brighton (SLB), Corinne, Ogden, Riverdale, and Snake Creek) in the GSL drainage were analyzed. Most of the precipitation in the GSL basin occurs in winter-spring. Precipitation increases with elevation. SLB, the highest available long-term precipitation station, is approximately at the elevation of the 700-mbar pressure surface. The SLB precipitation should be well correlated with precipitation-driven GSL fluctuations as well as larger-scale atmospheric fluctuations. Most of the GSL evaporation takes place in summer-fall. The summer diurnal temperature range near the GSL is of the order of 16°–22°C, with highs around 35°–40°C. The lowest temperature recorded in the GSL basin is −39°C, and the highest is 44°C for an extremal range of 83°C. Of the long-record stations available to us, the Corinne (COR) record was perhaps the most relevant for summer temperature-driven GSL fluctuations.

Three streamflow records (Table 1) were also analyzed. These records are believed to be free of any significant effects of reservoir regulation, diversion, or consumptive use [*Slack et al.*, 1992]. Blacksmith Fork is near the northern extreme of the GSL drainage, Weber River is in the middle, and Beaver River is south of the GSL drainage. The sources of moisture for Beaver River and Blacksmith Fork can be different depending on the location and configuration of the winter jet stream.

Willett and Prohaska [1985] speculate that three major circulation patterns influence the weather in the basin. These are (1) a high-latitude (50°N), moderate jet stream, corresponding to a dry climate; (2) a lower-latitude split jet stream, with a primary storm track that borders the northern extreme of the GSL drainage and a secondary storm track that borders the southern part of the drainage; and (3) a cellular blocking pattern with large, alternating north and south strong jets and a breakdown of the westerly flow. The split jet stream is very active and corresponds to a rapid rise of the GSL. The cellular blocking pattern leads to hot, dry summers and a falling GSL.

In their investigation of the relationship between North Pacific atmospheric circulation and streamflow in the western United States, *Cayan and Peterson* [1989] noted a strong association (correlation, 0.43) between positive Weber River streamflow anomalies and a positive sea level pressure (SLP) anomaly centered over the North Pacific with a negative SLP anomaly locally. This implies a southerly displaced storm track across the eastern North Pacific and into the west with increased activity from Canadian and Alaskan storms that dip in east of the Cascades. An anomalous northeasterly to southeasterly flow with precipitation associated with a local trough corresponds to this pattern. Enhanced winter precipitation is accompanied by positive minimum daily temperature anomalies. *Cayan and Peterson* [1989] found a positive association between the Southern Oscillation index (SOI) (defined as the difference between normalized SLP anomalies for Darwin and Tahiti) and two indices of pressure anomalies over the North Pacific, the Pacific North American (PNA) index (defined in terms of 700-mbar height H, as PNA = H(170°W, 20°N) − H(165°W, 45°N) + H(115°W, 58°N) − H(90°W, 30°N), and the central North Pacific (CNP) index (defined as CNP equals the average SLP over 35°–55°N and 170°E–150°W). These indices reflect characteristic pressure systems that determine atmospheric flow and hence precipitation in the GSL area. The SOI has nearly periodic behavior [*Keppenne and Ghil*, 1992] with high- (2–3 year) and low-frequency (4–7 year) bands corresponding to ENSO, which is best understood as an internal self-sustained equatorial oscillation in the coupled ocean-atmosphere system [see *Philander*, 1990]. Streamflow relates to PNA and CNP, which are measures of the strength of the winter Aleutian Low (see also *Barnston and van den Dool* [1993], who identify the GSL area as one with a minimum in interannual northern hemisphere 700-mbar height standard deviation). One should thus expect some organized interannual variability at least in the ENSO band for the hydroclimatic variables in this area.

Spectral Analysis Methods

The limited length of instrumental records, the sensitivity of the variable analyzed to local as well as global factors, the intermittence of oscillatory patterns, and issues (see MP93) related to the interpretation of space- and time-averaged data make the identification of a coherent long-period signal difficult. Spectral analysis methods tailored to the identification of coherent variability in specific frequency bands where the underlying spectrum may have line (i.e., sharp peaks corresponding to periodic behavior) as well as broadband (due to stochastic, chaotic, or nearly periodic factors) features are needed.

We tested windowed periodograms, maximum entropy spectral estimates (MESA), SSA, and MTM on a variety of synthetic data sets with these factors in mind. Of these, MTM and SSA were the most successful in terms of the criteria listed above. Our goal here is to present evidence of low-frequency climatic variability, rather than a comparative evaluation of methods of spectral estimation. We shall limit ourselves to a brief description of the relevant attributes of SSA and MTM.

We use SSA to identify anharmonic oscillations, and MTM for identification of peaks and frequency band structure.

Singular Spectral Analysis (SSA)

An excellent exposition of SSA, complete with guidance for interpretation of results, tests, and properties, is provided by *Vautard et al.* [1992]. Recall that the traditional periodogram constructs the spectrum as a Fourier decomposition of the variance of the time series. This can be done equivalently through appropriate Fourier transforms of the time series or the autocovariance function. Likewise, the windowing or smoothing operation can be done in the frequency, time, or autocovariance domain. SSA operates on the autocovariance structure of the time series. It differs in using data-driven, empirical, orthogonal basis functions, rather than Fourier (i.e., sin or cos) basis functions for the decomposition. *Ghil and Le Treut* [1981] discuss and model sawtooth-shaped variations in the Quaternary climate record, which could be captured better by SSA than the Fourier basis.

SSA considers the eigen decomposition (principal component analysis, PCA) of the autocorrelation matrix of a time series formed to some lag M. The resulting eigenvectors are the basis functions. The corresponding eigenvalues indicate the fraction of overall variance explained by an eigenvector, and projections of the time series on to the eigenvector provide a representation of that component of the time series. Eigenvectors with the same shape and nearly equal eigenvalues are called oscillatory pairs and jointly represent the amplitude and phase of a cyclic pattern. SSA can potentially resolve signal and noise and works well in situations where there is a distinct signal-noise separation. The data-driven basis functions can potentially resolve the signal in terms of a smaller set of basis functions than the Fourier basis. SSA can have problems identifying underlying signals if a long-memory stochastic process constitutes the noise or if the underlying signals have periods that are close, but long relative to reasonable choices of the windowing parameter (lag M). Its strength is the recovery of dominant, arbitrarily shaped, data adaptive recurrent patterns from a finite sample, and their corresponding time history. A decomposition of the time series into orthogonal variance components and their associated time patterns is provided. Thus one can identify the timing and amplitude of oscillations, as well as the nature of trends. The statistical machinery associated with PCA is readily invoked by SSA. A synopsis of the algorithm (based on *Vautard et al.* [1992]) for a scalar time series follows. While some results are referenced in this section, they are formally discussed later.

Toeplitz matrix. Given a time series $\{x_i, i = 1, \cdots, n\}$, translated to have zero expectation, and rescaled to unit standard deviation, form the Toeplitz matrix $\mathbf{T}_x$, with element $t_{ij} = c(k)$, where $k = |i - j|$, $k = 0, \cdots, M - 1$, and $c(k) = (1/(n - k)) \sum_{i=1}^{n-k} x_i x_{i+k}$ is an estimate of the lag k covariance. Here the dimension of $\mathbf{T}_x$ is $M \times M$, and M has the role of a smoothing window. The longest period recoverable is thus M. *Vautard et al.* [1992] recommend $M \leq n/3$ for stability of the computed $c(k)$. They also suggest that SSA is successful in analyzing periods in the range $(M/5, M)$. The spectral resolution is $1/M$ since the frequencies that can be resolved are $1, 1/2, \cdots, 1/k, \cdots, 1/M$. As M decreases, neighboring peaks in the spectrum may coalesce, while as M increases, a peak may split into components at adjacent frequencies (the Gibbs effect). Varying M over a coarse grid during the analysis is consequently desirable to screen out spurious frequencies and to focus on signals in different frequency bands.

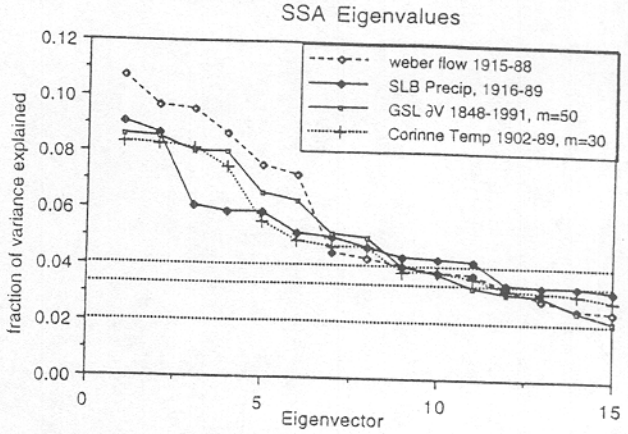

Figure 3. Eigenvalue spectra from SSA for selected sites. The window length $M = 25$ years unless noted otherwise. The three horizontal lines (0.02, 0.033, 0.04) correspond to the average eigenvalues for (WRO, SLB), COR-T, and GSL, respectively. Only the first 15 eigenvectors are shown in each case. Note the near equality of some pairs of leading eigenvalues (especially GSL). Typically, these pairs correspond to eigenvectors that are periodic and in quadrature as shown in Figure 4. Such a relation was not clear-cut for COR-T, where the first four eigenvalues are nearly equal and only the first and fourth eigenvector look "similar."

Eigen decomposition. An eigen decomposition of $\mathbf{T}_x$ yields a decomposition of the total variance into components in a manner analogous to Fourier analysis:

$$\mathbf{T}_x = \mathbf{E}^T \Lambda \mathbf{E} \tag{1}$$

where Λ is a diagonal matrix of eigenvalues (generally positive) sorted in descending order and $\mathbf{E}$ is a corresponding matrix of eigenvectors such that $\mathbf{E}^T\mathbf{E} = \mathbf{I}$.

Each eigenvector $\mathbf{e}_i$ of length M represents a data pattern, or empirical orthogonal basis function. The corresponding eigenvalue λ_i provides a measure of the variance associated with this pattern. The leading eigenvectors consequently provide information on the dominant patterns in the data. All eigenvalues for a white noise series are equal in expectation. A plot of λ_i versus i is termed an SSA eigenspectrum (see Figure 3 for some of our data sets). Eigenvectors i and $i + 1$ are termed an oscillatory pair if $\lambda_i \approx \lambda_{i+1}$, and the coefficients e_j^i and e_j^{i+1} exhibit a similar temporal pattern for $j = 1, \cdots, M$. *Preisendorfer* [1988, p. 247] reports that standard deviation $\partial\lambda_i$ of λ_i is asymptotically $\lambda_i(2/n)^{1/2}$. Thus if $(\lambda_i - \lambda_{i+1})$ is of the same size or smaller than $\partial\lambda_i$, the eigenvalues may be considered to be equal. One can think of this oscillatory pair (see Figure 4 for an example) as a sine and cosine pair that carries the frequency and phase information. Energetic intermittent oscillations with lifetime less than the window length can be identified through the eigencoefficient pattern.

A number of strategies for selecting the "statistically significant" eigenvectors for PCA are described by *Preisendorfer* [1988]. These are applicable here as well. GV, *Vautard et al.* [1992], and *Allen and Smith* [1994] review some of these techniques as well as Monte Carlo strategies for testing for significance against white and red noise. For the results presented here, we (1) considered only the first eight eigenvectors in any

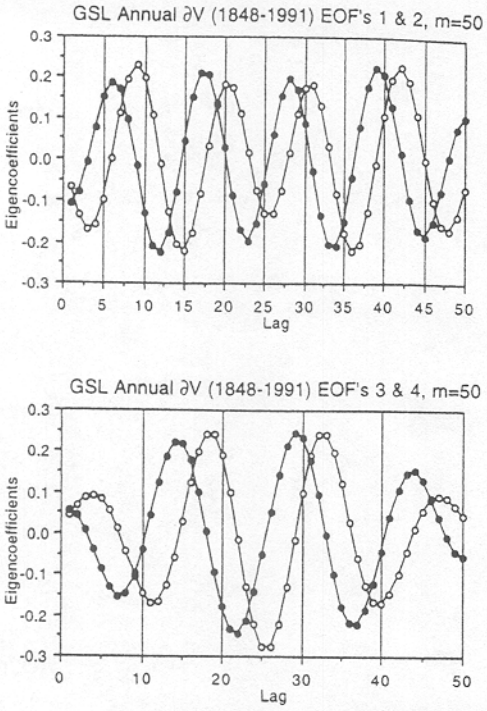

Figure 4. Eigenvectors 1–4 for annual GSL ∂V. Each set is seen to form an oscillatory pair (near 11 years for eigenvectors 1 and 2 and near 15 years for eigenvectors 3 and 4). Not all eigenvectors whose eigenvalues are nearly equal are so obviously in quadrature.

case, (2) dropped eigenvectors if the corresponding eigenvalue dropped below $1/M$, and (3) considered paired eigenvectors only as described above, where the patterns were distinct, meaningful, and similar. Finally, in line with the recommendations of *Allen and Smith* [1994], we satisfied ourselves that our choices were conservative relative to those from the significance criteria against a red noise hypothesis (using a modification of rule N, described by *Preisendorfer* [1988, pp. 199–206], based on a Monte Carlo analysis of Gaussian data, with consideration of serial correlation). Coherent patterns that have low contribution to the time series variance are thus missed. Our primary purpose for using SSA was to identify prominent recurrent patterns and their time projection, with a view to comparing the leading patterns in local precipitation, temperature, and the GSL. Formal significance testing of peaks was done as part of the MTM procedure.

Principal components. The principal components (PCs) of $\mathbf{T}_x$ are defined as

$$\mathbf{A} = \mathbf{XE} \tag{2}$$

where the matrix $\mathbf{X}$ is the $(n - M + 1) \times M$ matrix formed by augmenting the time series by $(M - 1)$ lagged copies of itself and $\mathbf{A}$ is an $(n - M + 1) \times M$ matrix of projections of $\mathbf{X}$ onto the space formed by the eigenvectors $\mathbf{E}$. Each PC $\mathbf{a}_j$, $j = 1, \cdots, M$, can be considered as a different weighted moving average or a filtered representation of length $(n - M + 1)$ of the process $\mathbf{x}$.

Reconstructed components. Noting that PCs are of length less than the time series, that a unique expansion of the signal in terms of the PCs is not possible, and that one is interested in seeing what the time series x_i looks like as filtered by a subset of the eigenvectors (e.g., an oscillatory pair), *Vautard et al.* [1992] define reconstructed components (RCs). Consider a partition $\mathbf{E}_K$ of $\mathbf{E}$ that contains the K eigenvectors that we wish to retain. The K could include the indices of one or more oscillatory pairs, or simply a particular eigenvector. The corresponding partition of $\mathbf{A}$ is $\mathbf{A}_K$. Now define the vector $\mathbf{r}_K$ of length n as the time series reconstructed from the original time series $\mathbf{x}$, corresponding to these K eigenvectors. Also define $\mathbf{R}_K$ as an augmented matrix of $\mathbf{r}_K$ formed in the same way as $\mathbf{X}$ was formed from $\mathbf{x}$. Now the reconstructed component $\mathbf{r}_K$ is obtained as the vector for which the matrix $\mathbf{R}_K$ is closest in a least squares sense to the projection of $\mathbf{X}$ onto $\mathbf{E}_K$. *Vautard et al.* [1992] report the solution as

$$r_{K,i} = \frac{1}{M} \sum_{j=1}^{M} \sum_{k \epsilon K} a_{i-j}^k e_j^k \qquad M \le i \le n - M + 1 \tag{3a}$$

$$r_{K,i} = \frac{1}{i} \sum_{j=1}^{i} \sum_{k \epsilon K} a_{i-j}^k e_j^k \qquad 1 \le i \le M - 1 \tag{3b}$$

$$r_{K,i} = \frac{1}{n - i + 1} \sum_{j=i-n+M}^{M} \sum_{k \epsilon K} a_{i-j}^k e_j^k \tag{3c}$$

$$n - M + 2 \le i \le n$$

Note that (3a) corresponds to the interior and (3b) and (3c) to the boundary regions. Recall that the standard PCA reconstruction formula given the eigen decomposition is $\mathbf{X} = \mathbf{AE}^T$. The *Vautard et al.* [1992] solution for RCs is obtained from the reconstruction $\mathbf{X}_K$ (using $\mathbf{A}_K$ and $\mathbf{E}_K$), by recognizing (1) that the matrix element $x_K(i, j)$, for $j > 1$, is really supposed to be an estimate of x_{i+j-1}, (2) that there are now up to M such estimates of each x_i, and (3) that the "optimal" solution is the simple average of these estimates for each time index i.

The RCs represent a data adaptive linear filter of the original data. There is no phase shift between $\mathbf{x}$ and $\mathbf{r}_K$ for oscillatory pairs. The original time series may be recovered exactly by adding up the M RCs. Say that K represents the indices of an oscillatory pair identified above ("eigen decomposition" subsection). Then $\mathbf{r}_K$ represents the optimal projection of the time series onto that oscillatory pair; i.e., it shows what that component pattern looked like over time. Time plots of $\mathbf{r}_K$ (i.e., $r_{K,i}$ versus i, $i = 1, \cdots, n$) are useful for identifying whether the oscillation was intermittent or continuous and determining its amplitude variations and regularity. Examples of such reconstructions are presented in Figures 5 and 6.

Multitaper Method of Spectral Analysis (MTM)

Thomson [1982] provides the following motivation for the MTM algorithm. He points out that (1) the classical periodogram is an inconsistent estimator of the spectrum; (2) without a taper window it may be too biased to be useful; (3) usual tapers can reduce variance efficiency; (4) smoothing the periodogram is unsatisfactory for spectra with large range and line and broadband components, since the true spectrum is not smooth; and (5) since the periodogram-based spectral estimator does not directly use phase information, line detection is poor. He sets his sights on developing an estimator (MTM) that (1) is consistent, (2) has good small-sample performance in terms of variance efficiency, (3) is data adaptive, (4) is nonparametric, i.e., locally approximates the spectrum using information only from neighboring frequencies, (5) works well

with spectra with a high dynamic range, (6) is computationally easy, and (7) has statistics that can be estimated so that significance tests for line components and coherence can be provided. We outline the aspects of the MTM algorithm relevant to our presentation and refer the reader to *Thomson* [1982] and *Percival and Walden* [1993, chap. 7] for details.

The finite discrete Fourier transform (DFT) of the data, $x(0), \cdots, x(t), \cdots, x(n-1)$ is given by

$$y(f) = \sum_{t=0}^{n-1} e^{-i2\pi f(t-(n-1)/2)} x(t) \tag{4}$$

For a finite data set, the DFT is related to the spectrum as

$$y(f) = \int_{-1/2}^{1/2} \frac{\sin n\pi(f-v)}{\sin \pi(f-v)}\, dZ(v) = \int_{-1/2}^{1/2} G(n, f, v)\, dZ(v) \tag{5}$$

where the spectrum $S(f)$ is defined through $\{S(f)\, df = E[|dZ(f)|^2]\}$, where $E[\ \ ]$ denotes expectation.

Note that the periodogram estimate $S_p(f)$ is simply $|y(f)|^2$, whose properties will not correspond to those of $S(f)$, since the term $G(n, f, v)$ in (5) poorly approximates a Dirac delta function. This term is a consequence of a rectangular window of width n placed on the underlying process. Given the estimate $y(f)$, one can seek a solution for $dZ(f_0)$ in (5) in some locale $(f_0 - W, f_0 + W)$ of a frequency f_0. This is an inverse problem parameterized by $G(n, f, v)$. Thomson pursues a least squares solution by considering a weighted eigenfunction expansion in this locale and then an appropriate combination of the resulting estimates. Consider the K term $(k = 0, \cdots, K-1)$ eigenfunction expansion:

$$\lambda_k(n, W) U_k(n, W; f) = \int_{-W}^{W} G(n, f, v) U(n, W; v)\, dv \tag{6}$$

where $U_k(n, W; f)$ is the kth eigenfunction centered at f, with window width W, and $\lambda_k(n, W)$ is the corresponding eigenvalue.

The eigenfunctions (called discrete prolate spheroidal wave functions) are ordered by decreasing eigenvalue, with the first nW eigenvalues close to 1. Consequently, of all functions that are DFTs of some discrete sequence, these leading eigenfunctions have a maximum energy concentration in the interval $(f_0 - W, f_0 + W)$. This implies that the tapers are leakage resistant. The window width W is $0 < W < \frac{1}{2}$, and is usually of order $1/N$ to retain high resolution of the resulting estimate. The idea here is that if the K term approximation in (6) is "good," then a good solution to the estimation of $S(f)$ is available. Thomson derives such a solution by first considering K spectral estimates corresponding to each of the eigenfunctions and then combining them using an optimality criterion derived from estimates of the mean square error of estimate of the spectrum in the locale of interest. The K eigenspectra $S_k(f)$, $k = 0, \cdots, K-1$, are defined through

$$y_k(f) = \sum_{t=0}^{n-1} x(t)\, \frac{v_{t,k}(n, W)}{\varepsilon_k}\, e^{-i2\pi f(t-(n-1)/2)} \tag{7}$$

$$S_k(f) = |y_k(f)|^2 \tag{8}$$

where ε_k is 1 for k even, and i for k odd; and $v_{t,k}(n, W)$, the kth discrete prolate spheroidal sequence (DPSS), is defined such that its Fourier transform gives $U_k(n, W; f - f_0)$.

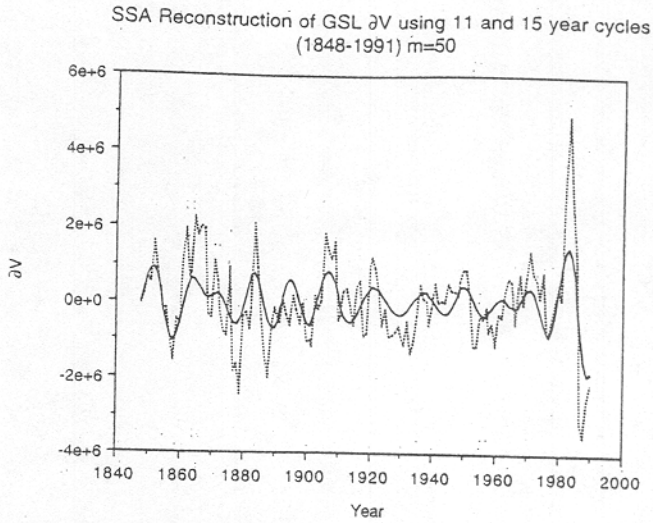

Figure 5. Reconstruction (solid curve) of annual GSL ∂V time series (dotted curve) using the 11- and 15-year cycles shown in Figure 4. Nearly 33% of the variance is accounted for.

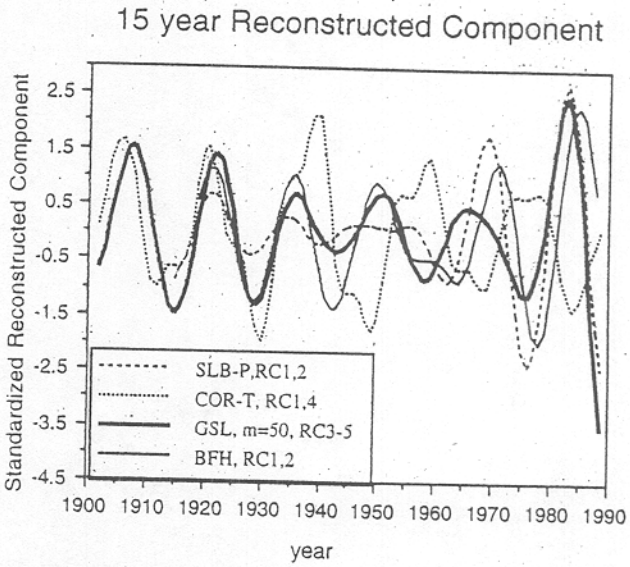

Figure 6. Comparison of 15-year reconstructed component pair (RCP) of annual GSL ∂V, SLB-P, COR-T, and BFH. To ease plotting, each RCP is standardized by removing its mean and dividing by its standard deviation. In each case the full record described in Table 1 was used. Results are plotted only for the overlapping time period. Each RCP has an approximately 14–15 year period. Note how the GSL and precipitation (SLB-P) are nearly coherent throughout, while the temperature (COR-T) signal is nearly in phase with the other two to begin with and then drifts completely out of phase around 1950. The COR-T eigenvectors corresponding to this RCP were not as clearly periodic as the others; and this RCP may represent a mixture of two nearby interdecadal frequencies, resulting in a "frequency" drift. The streamflow BFH is also coherent with GSL and SLB-P. Evidence of a phase drift between GSL and BFH in the 1960–1989 period is also evident. However, this drift may be due to the estimated periods' being slightly different. The maximum correlation of GSL ∂V with SLB-P is 0.76 at lag 0, with COR-T is −0.1 at lag 1, and with BFH is 0.71 at a lag of −2 years. SLB-P and COR-T have a lag 0 correlation of −0.29.

The MTM estimate is obtained as

$$S_M(f) = \sum_{k=0}^{K-1} w_k(f) S_k(f) \tag{9}$$

and $w_k(f)$ is a weight associated with the kth eigenspectrum estimate at frequency f.

The windows $U_k(\ )$ are positive everywhere, and hence the problem of getting negative estimates of $S(f)$ resulting from traditional higher-order spectral windows is averted. The combined estimate from K orthogonal tapers also circumvents the loss of resolution and variance efficiency problems endemic to periodograms smoothed with a single taper. The orthogonality of the eigenfunctions leads the S_k to be approximately uncorrelated. MTM recovers information lost by using a single taper and by ignoring the phase information in the periodogram. A number of strategies for choosing the weights $w_k(f)$ at each frequency f are indicated by Thomson. These include a simple average, weights proportional to the eigenvalues λ_k, and a fully data adaptive and recursive procedure that internally estimates the bias and variance of the local estimate. We used the last two strategies in our work. The latter allows improved separation of the line and broadband spectral components. We refer the reader to Thomson for details of the DPSS and the w_k and discuss the choice of W and K, the user-selected parameters of the model.

The half bandwidth W is usually specified in terms of the Rayleigh frequency $f_R = (n\Delta t)^{-1}$, where Δt is the sampling frequency, as pf_R, where p is usually a small integer. The corresponding DPSS is called a $p\pi$ taper. The corresponding spectral estimate averages in the frequency band $f \pm pf_R$. For example, a 2π taper for a 100-year annual data set would average over $f \pm 0.02$ cycles/year. Note that this would correspond to periods of 1.92–2.08 years for a band centered at $f = 0.5$, and 14.28–33.33 years for a band centered at $f = 0.05$. We see from this example that it is desirable to use a small value of p to get higher resolution in the low-frequency range. On the other hand, a small value of p can lead to peak splitting in the high-frequency range. Comparing estimates obtained by varying p over a small range is consequently desirable. As K increases, the variance of S_M decreases; however, the bias can increase owing to increased smoothing. S_M is distributed as χ^2_{2K}, rather than as χ^2_2 for the periodogram, and the increased degrees of freedom correspond to reduced variance. The first $(2p - 1)$ tapers are leakage resistant, so K is usually taken to be $2p - 1$. As p increases, the number of leakage resistant tapers increases. Note that as n increases, one can increase p while retaining the same spectral resolution. The estimate $S_M(f)$ is unbiased, but its local features (amplitude) will depend on p and K. Consequently, it is desirable to also look at a significance test for line components based on the ratio of variance explained by a peak at f_0 to unexplained variance in a band centered at f_0.

Thomson shows that an F variance ratio test with 2 and $2K - 2$ degrees of freedom can be constructed for significance of line components through the statistic $F(f)$:

$$F(f) = \frac{(K-1)|\mu(f)|^2 \sum_{k=0}^{K-1} U_k(n, W; 0)^2}{\sum_{k=0}^{K-1} |y_k(f) - \mu(f) U_k(n, W; 0)|^2} \tag{10}$$

where

$$\mu(f) = \frac{\sum_{k=0}^{K-1} U_k(0) y_k(f)}{\sum_{k=0}^{K-1} U_k^2(0)} \tag{11}$$

Vautard et al. [1992] point out that the maxima of $S_M(f)$ and $F(f)$ do not always coincide and suggest using the maxima of $F(f)$ for peak identification. We examined $S_M(f)$ for the different time series analyzed to identify any clear-cut bands with high values of $S_M(f)$. Then we assessed the total power (integral of $S_M(f)$) in each such band and ranked the importance of each such band for each time series. Finally, we examined $F(f)$ to identify any peaks that passed the 99% significance test in each time series.

The coherence $C(f)$ across two time series $x_t^{(1)}$, $t = 0, \cdots, n - 1$, and $x_t^{(2)}$, $t = 0, \cdots, n - 1$, is estimated as

$$C(f) = \frac{\sum_{k=0}^{K-1} y_k^{(1)*}(f) y_k^{(2)}(f)}{\left(\sum_{k=0}^{K-1} y_k^{(1)*}(f) y_k^{(1)}(f) \sum_{j=0}^{K-1} y_j^{(2)*}(f) y_j^{(2)}(f) \right)^{1/2}} \tag{12}$$

where an asterisk represents a complex conjugate. A confidence test [see *Brillinger*, 1981] similar to the F variance ratio test is used to test for the significance of the coherence amplitude.

Our experience with synthetic data suggested that the MTM procedures were very reliable and were not as sensitive to signal to noise ratio or to the memory in the broadband noise process as SSA or MESA or periodogram estimates. We did not see a need to prefilter the data via SSA and then apply MTM, as done by *Vautard et al.* [1992]. The reader may have noted that SSA uses an eigenexpansion of the autocovariance function, while MTM does something similar in the frequency domain. Consequently, SSA may be more useful for showing time patterns. MTM is generally superior for identifying phase coherent frequency structure. One could subject the SSA RCs to frequency analysis by MTM or use the MTM estimates in the frequency domain to band pass the time series at desired frequencies. We prefer to examine the SSA time optimal decompositions and the MTM frequency optimal decomposition independently and seek consistency across the analyses. Confirmation of "patterns" by independent analyses by different methods and across data sets is in our view more valuable than statistical confidence limits for a single analysis of a particular data set. A comparative discussion of the two methods is offered by *Thomson* [1982] and *Vautard et al.* [1992].

Spectral Analysis Results

For brevity we shall focus on the main points through an examination of some key spectra and through the summary of the individual time series analyses presented in Table 2. After a preliminary screening of the spectral output, it was clear that one could designate bands in which there was power. The bands are larger in the time domain near the lower frequencies recognizing the increasing effect of the fixed averaging window in frequency space. The approximate spectral power in each band was ranked for each time series, and any spectral peak in

Table 2. Results From Spectral Analysis

Data Set	Period							Total Percent Variance
	2–3 years	3–5 years	5–8 years	8–10 years	10–12 years	12–25 years	Longer	
MTM Results								
GSL M^1	7 (2, 2.3, 2.6)	4 (3.2, 3.5, 5)	6 (6)	5	2 (12)	1 (20)	2	
SNC-P M^2	2 (2.8)	4 (4.6)	1 (7)			3 (>20)		
SLB-P M^2	1 (2.3, 2.7)	2 (3.3, 4.6)	3 (7)		4	5 (21, 14)		
RIV-P M^2	2 (2.8)	3 (3.6, 4.4)	5 (7)	5	5 (10)	3	1	
OGD-P M^2	1 (2, 2.3)	2 (3.9, 5.3)	4 (6)		3 (12)	5 (14.8)	2	
COR-P M^2	3 (2.3)	1 (3.3, 3.8, 4.7)	4		5 (9.8)	6	2	
SNC-T M^2	4 (2.2, 2.6)	1 (4.6)	5 (6.8, 7.7)			2 (16)	3	
COR-T M^2	3 (2.5)	2 (3.1, 4, 4.8)	3 (6.7)			1 (17.5)		
RIV-T M^2	4 (2.2, 2.7)	2 (3.3, 4.7)			1 (10)	3 (17, 24)		
BRB M^2	3 (2.4, 2.8)	1 (3.2, 4.2)		5 (9)		2 (21)	4	
WRO M^2	5 (2.2, 2.7)	3 (3.3, 3.6)	2 (5.8)		1 (12)	4 (25)		
BFH M^2	6 (2.3, 2.8)	5 (3.3, 4.8)	4 (5.7, 7)		3	1 (21)	2	
SSA Results								
GSL S(25)		9% (4.5)		24% (8–9)	21% (12)			54%
GSL S(50)				14% (8–9)	17% (11)	16% (15)	5% (35)	59%
SLB-P S(25)		8% (3)				18% (14)		26%
COR-T S(30)		12% (4)	16% (6)			16% (15)		44%
BRB S(25)		29% (5, 4)				15% (14)		44%
WRO S(25)		22% (4, 5)	14% (7.5)			15% (18)		51%
BFH S(25)			17% (7)			21% (13–14)		38%

Data sets referring to precipitation records end in "-P"; those referring to temperature records end in "-T." M^1 denotes data sets based on MTM with six 4π and three 2π tapers; M^2 denotes data sets based on MTM with three 2π and two 1π tapers. For MTM the entries for each band represent rank of spectral power for the band; the values in parentheses are the peaks that were significant from an F test at 99%. The rank is based on the integral of the spectrum over the band. The band with the most power is ranked 1. The data sets marked with an $S(\ )$ denote SSA results for a value of M given in parentheses. For SSA the variance given is for an oscillatory pair, followed by the indicated period in parentheses. All SSA were computed with annual values, and all MTM with monthly values. GSL is differenced; others are not. The window M in SSA is chosen toward $n/3$ to (1) better resolve low frequencies and (2) reduce the effect of leakage of high power from the Nyquist frequency (in this case 2 years). SSA is expected to resolve periods in the range $[M/5, M]$.

that band that met the F variance ratio test for significance at the 0.99 level for MTM was also recorded. For a confident interpretation of a periodic signal, it is desirable to have sizable power as well as a significant F test. Features that are resistant to the indicated variations in MTM parameters are reported in Table 2. We summarize results for the GSL, all precipitation series, all temperature series, and then all streamflow series. In each subset, sites are arranged from south to north. The SSA results report the fractional variance explained by the oscillatory pairs of eigenvectors and the corresponding period of the variation. Only the readily interpretable eigenvectors, with dominant eigenvalues, are used. The last column for the SSA results gives the total variance explained by the selected eigenvectors.

Representative MTM spectra for each hydroclimatic process are presented in Figures 7–10. MTM estimates of coherence across selected time series are presented in Figures 11–13.

We offer the following observations:

1. There is significant power in these series at selected bands. There are also clear gaps in the spectrum at some frequency bands (e.g., 8–10 years). Such features are generally consistent across sites for the same type of series, in particular for sites at similar elevation and latitude.

2. Coherent cyclic activity with periods around 2.2, 2.6, 2.8, 3.3, 3.6, 3.9, 4.5, 5, 6, 7, 10, 14, 17, and 21 years shows up in the MTM analysis of virtually all the series. These cycles are consistent with the summary presented in our motivational section. These frequencies are best interpreted as representing activity in the bands shown in Table 2. Support for the 14- to 15-year cycle and the lower-frequency end of the ENSO band also comes from the SSA analysis of each time series. We report fewer cycles from SSA because we were rather deliberate about excluding eigenvectors with low variance even if they showed coherent patterns.

3. A small set of low-frequency recurrent patterns explains a relatively large fraction of the observed variability for some time series. As an example, see Figure 5 for a reconstruction of the GSL series using only the 11- and 15-year cycles that account for 33% of the variance in the series. It is worth noting that significant modes of spatiotemporal variance in global surface temperature are observed on each of these timescales in MP94. GV report 15- and 20-year cycles in global average temperature, while MP94 identify a broader-band 16- to 20-year oscillation in gridded surface temperature records.

4. The relative amplitude of these cycles varies across the

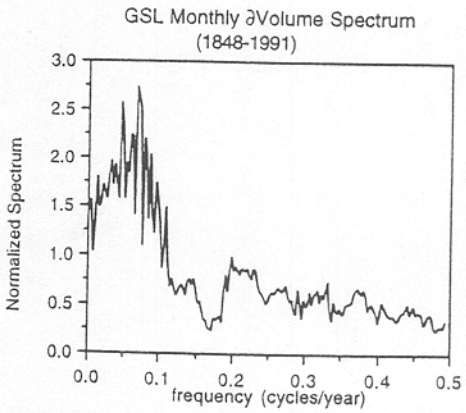

Figure 7. Normalized MTM spectrum of GSL monthly volume change (using six 4π tapers).

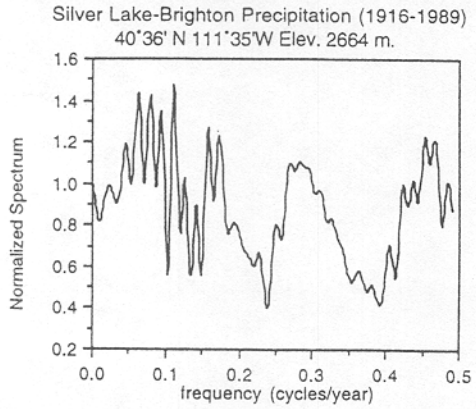

Figure 8. Normalized MTM spectrum of SLB precipitation (using three 2π tapers).

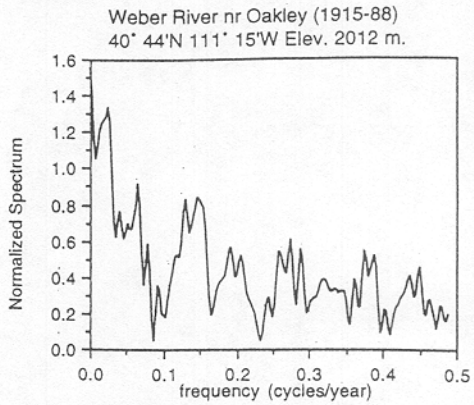

Figure 10. Normalized MTM spectrum of WRO (three 2π tapers).

series, with the GSL series favoring the lower frequencies as expected. A closer examination of these series (e.g., Figure 6) reveals that the amplitude of each cycle is variable over each record as well.

5. The MTM spectra for precipitation and temperature data from Corinne, Ogden, and Riverdale (only Corinne is shown here) are very similar, reflecting the proximity of these sites to each other and the consistency of the local signal.

6. The frequencies identified by SSA and MTM for a given time series are usually similar, but not identical. The frequency bands identified are consistent. MTM peaks appear to pick the "middle" period range of the broader-band SSA. There is also consistency across time series for a given method. The differences by method are likely due to differences in the windowing/smoothing parameters used and also arise because SSA is time optimal and MTM frequency optimal. The different values of M used for SSA isolate somewhat different frequency bands. Our selections for Table 2 in both cases were quite restrictive. Relaxing the criteria leads to more commonality in the signals identified here, as well as additional frequencies.

A graphical depiction of the relationship between long-term precipitation, temperature, and GSL variability is offered in Figure 6, which shows the projections of the respective time series on the near 15-year oscillatory pair identified by SSA. It is encouraging that independent analyses of these time series show a very similar pattern. Note the close correspondence between the time pattern of the 15-year cycle in precipitation and annual GSL ∂V. In the early part of the record, the temperature signal appears to be in phase with the precipitation and annual GSL ∂V. However, in the 1950s the precipitation cycle has near-zero amplitude, and the temperature signal loses its phase completely. Similarly, the BFH streamflow RC, which follows the GSL RC closely in the early part of the record, seems to drift in phase in the latter 20 years. This is reminiscent of our earlier discussion regarding the attributes of a nonlinear system. At the end of the time series, we have negative temperature anomalies for this cycle coinciding with positive anomalies in precipitation and annual GSL ∂V. What is the explanation for coincident positive anomalies in all series that we see in the earlier part of the record? Recall that the SSA analysis was performed with annual data. Seasonal effects are consequently masked. A warmer winter may very well be associated with increased sensible heat and moisture fluxes associated with a southwesterly flow. On the other hand, a milder summer would clearly correspond to a positive lake anomaly. We suspect that the two conditions correspond to persistent large-scale circulation regimes that were set up preferentially during these periods. Of course, these arguments presume that the low-frequency temperature forcing is important for GSL ∂V, at least on the decadal timescale.

From Figure 5 we see that the combined 11- and 15-year

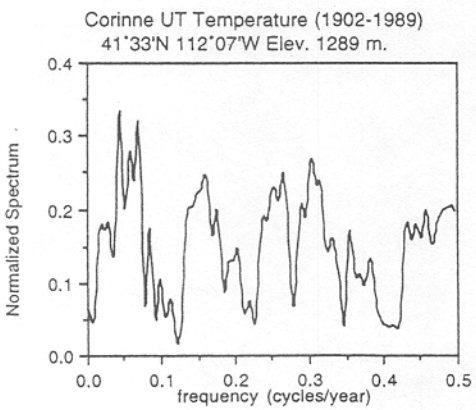

Figure 9. Normalized MTM spectrum of COR temperature (using three 2π tapers).

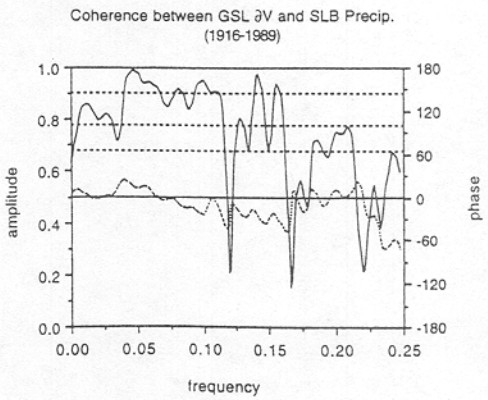

Figure 11. MTM coherence (solid curve) and phase (dotted curve) between monthly GSL ∂V and SLB-P, using three 2π tapers. The dashed horizontal lines are the 90%, 95%, and 99% confidence limits for coherence.

patterns appear to be visually convincing as appropriate moving averages or low-frequency filters for the data. Here it is worth reiterating the point of accounting for such variability in hydroclimatic models and data interpretation.

Let us examine our representative MTM spectra. Comparing Figures 7 and 8, the GSL spectrum appears to be a filtered version of the SLB precipitation spectrum, with the higher frequencies attenuated. Mechanistically, this is precisely what we expect. The transfer function of such a filter is not estimated here. We can also see qualitative similarities between the SLB precipitation and the COR temperature spectrum. The Weber River (Figure 10) spectrum is also similar with a bit more lower-frequency character than the precipitation or temperature, but not as clearly as for the monthly GSL ∂V. Streamflow and lake volume change are similar processes. However, the WRO gauge samples a much smaller fraction of the basin than the GSL and will thus represent a smaller amount of time and space averaging. Some of the differences in these spectra may be accounted for by noting that the GSL record is considerably longer, leading to a better ability to resolve lower frequencies.

Is the GSL essentially mirroring large-scale climatic variability, or is it showing interesting basin dynamics? Can we quantify the role of precipitation and temperature in the long-term evolution of the GSL? We have presented some discussion of this issue in reference to Figure 6. At this point we shall focus on coherence between the GSL, precipitation, temperature, and streamflow at low frequencies (<0.25 cycles/yr). From Figure 11 we see that there is very high coherence between SLB precipitation and GSL ∂V at virtually all frequencies (gaps correspond to spectral gaps in each series). Interestingly, the coherence increases with decreasing frequency and with a small phase lag. This suggests that low-frequency precipitation variability largely drives the GSL. From Figure 12 we observe that coherence between COR temperature and monthly GSL ∂V is high for three frequency bands (>40 years or secular, ≈10 years or decadal, ≈5 years or interannual). It is worth noting that these are precisely the three low-frequency bands where consistent climate signals impacting on the United States are noted through a spatiotemporal analysis of global surface temperatures and North American surface sea level pressures [*Mann et al.*, 1995]. Temperature is nearly 180° out of phase with the GSL ∂V. Recall that the COR-T MTM spectrum does not show much power at the 10-year period. A weak (in terms of variance) 10-year pattern in temperature nevertheless appears to be coherent with the 10-year GSL variability. From Table 2 we see that the COR-P precipitation does show a peak (which passes the F test) near 10 years in the MTM spectrum. The story is confirmed in Figure 13, where COR-T and SLB-P show a similar relationship to COR-T and monthly GSL ∂V. Given the analyses of global and U.S. data reported by *Mann et al.* [1995] and the results in Table 2 and Figures 11–13, we believe that the lake is largely precipitation driven, with temperature forcing important at a few selected frequencies. The temperature signals are consistent with the precipitation signals. A consistent climatic signal driving the long-term evolution of the GSL is thus apparent.

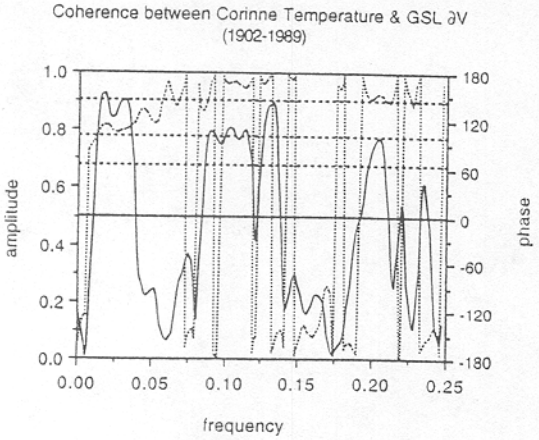

Figure 12. MTM coherence (solid curve) and phase (dotted curve) between GSL ∂V and COR-T, using three 2π tapers. The dashed horizontal lines are the 90%, 95%, and 99% confidence limits for coherence amplitude. Note that phase lags of 180° and −180° are the same, and switching between them may not be significant. The phase difference at $0.01 < f < 0.05$ has temperature leading GSL.

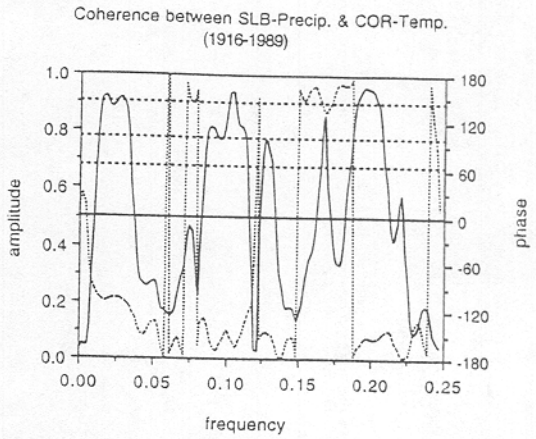

Figure 13. MTM coherence (solid curve) and phase (dotted curve) between SLB-P and COR-T, using three 2π tapers. The dashed horizontal lines are the 90%, 95%, and 99% confidence limits for coherence amplitude. Note that phase lags of 180° and −180° are the same, and switching between them may not be significant. The phase difference at $0.01 < f < 0.05$ has temperature leading SLB-P, as was the case with GSL.

A better understanding of the mechanisms responsible for this low-frequency climate variability is important for improved management of regional, anomalous wet periods and droughts and the rise and fall of the GSL. Work on linking these analyses with analyses of large-scale atmospheric circulation is reported by *Mann et al.* [1995]. Explanations for the apparent phase lag at low frequencies between temperature, precipitation, and GSL (Figures 12 and 13) are developed by *Mann et al.* [1995] in terms of the large-scale circulation. However, it is clear that the near 0° phase lag between SLB-P and monthly GSL ∂V, together with statistically significant coherence at some frequencies, is consistent with precipitative forcing of the GSL. Likewise, a 180° phase and significant coherence between monthly GSL ∂V and COR-T at certain frequencies may imply temperature forcing of GSL evaporation. The relationship with precipitation is present over a much larger fraction of the frequency range than the one between temperature and the GSL. Precipitative forcing may consequently account for far more of the low-frequency variability, and some of this variability appears to have periodic or quasi-periodic structure.

Conclusions

We find consistent evidence for structured low-frequency variability from an analysis of a number of hydroclimatic time series in the Great Salt Lake basin. The implications of such a finding were stressed earlier. Given the richness of the behavior seen, it is hard to accept simple explanations of external forcing at 11- and 18.6-year periods corresponding to the sunspot or lunar tide cycles, as advanced by some researchers (e.g., Willett and Prohaska, and Currie and O'Brien).

We also looked for seasonal attributes of the low-frequency variations. The main conclusions were that the larger variance of winter tends to weight things more, so that the modes are primarily a reflection of winter season variability. The quasi-decadal and secular signals have a similar character based on separate analyses of cold (OCT-MAR) and warm (APR-SEP) seasons. Other signals (e.g., ENSO) seemed to have a stronger seasonal character to them. The most important point is that the relevant peaks in the spectra for the quasi-decadal and secular signals were independent of the warm/cold seasonality, and the weighting of cold season variance is appropriate given the seasonality of precipitation in the GSL region.

The climatic behavior observed seems more consistent with the signature of a nonlinear dynamical system as discussed earlier: general broadband structure, with preferred frequency bands; with a variety of harmonics with power in a finite record; with lower frequencies being more important; with phase degeneracy of some signals; with amplitude of the harmonic variable dependent on position in the cycle; and with the hint of persistent low-frequency regimes marked by different joint characteristics of precipitation and temperature. Of course, this is a speculative argument, and in this manuscript we report no evidence of formal tests of nonlinearity (e.g., higher-order spectra or dimensionality or predictability). However, such evidence is presented in the work by *Sangoyomi* [1993] for the GSL time series.

The suggestion that low-frequency behavior accounts for a large part of the GSL variability and that this low-frequency signature is closely coupled to precipitation and temperature variability is also interesting. Recall that SLB, our index precipitation station, is a high-elevation station and is believed to be minimally affected by local factors such as lake effect precipitation. The high coherence between SLB-P and GSL ∂V at interannual and interdecadal periods has directed our efforts into seeking an understanding of the large-scale atmospheric circulation and its relation to low-frequency local precipitation and temperature variability [see *Mann et al.*, 1995]. Preliminary analyses suggest strong coherence between decadal and secular variations in spatial pressure and temperature fields and the GSL. This gives us hope that we can develop a cogent explanation for long-term GSL variability in terms of recurrent regimes that can be described for atmospheric circulation. Mechanistic investigations to develop a physical explanation for the observed low-frequency hydroclimatic variability should be fruitful and are being pursued.

Acknowledgments. We thank Barry Saltzman for helpful comments regarding the manuscript. U. Lall is grateful for support under NSF grant EAR-9205727 and USGS grant 1434-92-G-226, and to BSA, USGS, Reston, Virginia, for partial support of his sabbatical leave. M. Mann was supported by NASA grant NAG5-2316. An anonymous reviewer's comments were helpful in improving the manuscript.

References

Abarbanel, H. D. I., M. I. Rabinovich, and M. M. Sushchik, Introduction to nonlinear dynamics for physicists, World Sci., Singapore, 1993.

Allen, M. R., and L. A. Smith, Investigating the origins and significance of low-frequency modes of climate variability, *Geophys. Res. Lett.*, *21*, 883–886, 1994.

Barnston, A. G., and H. M. van den Dool, Toward understanding the causes of low-frequency variability: The interannual standard deviation of monthly mean 700-mb height, *J. Clim.*, *6*, 2083–2102, 1993.

Brillinger, D. R., *Time Series, Data Analysis and Theory*, Holden-Day, Oakland, Calif., 1981.

Burroughs, W. J., Weather cycles: Real or imaginary?, 201 pp., Cambridge Univ. Press, New York, 1992.

Cayan, D. R., and D. H. Peterson, The influence of North Pacific atmospheric circulation on streamflow in the West, in *Aspects of Climate Variability in the Pacific and the Western Americas*, *Geophys. Monogr. Ser.*, vol. 55, edited by D. H. Peterson, AGU, Washington, D. C., 1989.

Cayan, D. R., and R. Webb, El Nino/Southern Oscillation and streamflow in the western United States, in *El Niño: Historical and Paleoclimatic Aspects of the Southern Oscillation*, edited by H. F. Diaz and V. Markgraf, pp. 29–68, Cambridge Univ. Press, New York, 1992.

Currie, R. G., and D. P. O'Brien, Deterministic signals in USA precipitation records, II, *Int. J. Climatol.*, *12*, 181–304, 1992.

Dettinger, M. D., and M. Ghil, Interannual and interdecadal variability of surface-air temperatures in the United States, paper presented at 16th Annual Climate Diagnostics Workshop, Natl. Oceanic and Atmos. Admin., Los Angeles, Calif., 1991.

Diaz, H. F., and R. S. Pulwarty, An analysis of the time scales of variability in centuries-long ENSO-sensitive records in the last 100 years, *Clim. Change*, *26*, 317–342, 1994.

Fan, Y., and C. J. Duffy, Monthly temperature and precipitation fields on a storm-facing mountain front: Statistical structure and empirical parameterization, *Water Resour. Res.*, *29*(12), 4157–4166, 1993.

Ghil, M., and H. Le Treut, Climate model with cryodynamics and geodynamics, *J. Geophys. Res.*, *86*, 5262–5670, 1981.

Ghil, M., and R. Vautard, Interdecadal oscillations and the warming trend in global temperature time series, *Nature*, *350*, 324–327, 1991.

Guetter, A. K., and K. P. Georgakakos, River outflow of the conterminous United States, 1939–1988, *Bull. Am. Meteorol. Soc.*, *74*, 1873–1891, 1993.

Houghton, R. W., and Y. M. Tourre, Characteristics of low-frequency sea surface temperature fluctuations in the tropical Atlantic, *J. Clim.*, *5*, 765–771, 1992.

Jin, F.-F., J. D. Neelin, and M. Ghil, El Niño on the devil's staircase: Annual subharmonic steps to chaos, *Science*, *264*, 70–72, 1994.

Kahya, E., and J. A. Dracup, U.S. streamflow patterns in relation to the El Nino/Southern Oscillation, *Water Resour. Res.*, *29*(8), 2491–2503, 1993.

Keppenne, C. L., and M. Ghil, Adaptive filtering and prediction of the Southern Oscillation index, *J. Geophys. Res.*, *97*, 20,449–20,454, 1992.

Levitus, S., Interpentadal variability of temperature and salinity at intermediate depths of the North Atlantic Ocean, 1970–1974 versus 1955–1959, *J. Geophys. Res.*, *94*, 6091–6131, 1989.

Lorenz, E. N., Nondeterministic theories of climatic change, *Quat. Res.*, *6*, 496–506, 1976.

MacDonald, G. J., Spectral analysis of time series generated by nonlinear processes, *Rev. Geophys.*, *27*, 449–469, 1989.

Mann, M. E., and J. Park, Spatial correlations of interdecadal variation in global surface temperatures, *Geophys. Res. Lett.*, *20*, 1055–1058, 1993.

Mann, M. E., and J. Park, Global scale modes of surface temperature variability on interannual to century timescales, *J. Geophys. Res.*, *99*, 25,819–25,833, 1994.

Mann, M. E., U. Lall, and B. Saltzman, Decadal-to-century scale climate variability: Insights into the rise and fall of the Great Salt Lake, *Geophys. Res. Lett.*, *22*, 937–940, 1995.

Percival, D. B., and A. T. Walden, *Spectral Analysis for Physical Applications: Multitaper and Conventional Univariate Techniques*, Cambridge Univ. Press, New York, 1993.

Preisendorfer, R. W., *Principal Component Analysis in Meteorology and Oceanography*, 401 pp., Elsevier, New York, 1988.

Ropelewski, C. F., and M. S. Halpert, Global and regional scale pre-

cipitation patterns associated with the El Nino/Southern Oscillation, *Mon. Weather Rev.*, *115*, 1606–1626, 1987.

Saltzman, B., Climatic systems analysis, *Adv. Geophysics*, *25*, 173–233, 1983.

Sangoyomi, T. B., Climatic variability and dynamics of Great Salt Lake hydrology, Ph.D. dissertation, 247 pp., Utah State Univ., Logan, 1993.

Slack, J. R., J. M. Landwehr, and A. Lumb, A. U.S. Geological Survey streamflow data set for the United States for the study of climate variations, 1874–1988, U.S. *Geol. Surv. Open File Rep.*, *92-129*, 1992.

Thomson, D. J., Spectrum estimation and harmonic analysis, *IEEE Proc.*, *70*, 1055–1096, 1982.

Trenberth, K. E., Recent observed interdecadal climate changes in the northern hemisphere, *Bull. Am. Meteorol. Soc.*, *71*, 988–993, 1990.

Vautard R., P. Yiou, and M. Ghil, Singular spectrum analysis: A toolkit for short, noisy and chaotic series, *Physica D*, *58*, 95–126, 1992.

Willett, H. C., and J. T. Prohaska, The prediction of the future water levels of the Great Salt Lake, in *Cenozoic Geology of Western Utah—Sites for Precious Metal and Hydrocarbon Accumulations, Utah Geol. Assoc. Publ.*, *16*, 1985.

U. Lall, Utah Water Research Laboratory, Box UMC82, Utah State University, Logan, UT 84322-8200. (e-mail: ulall@kernel.uwrl.usu.edu)

M. Mann, Department of Geology and Geophysics, Yale University, P. O. Box 208109, New Haven, CT 06520-8109.

(Received October 24, 1994; revised June 12, 1995; accepted June 22, 1995.)